Modelling built-settlements between remotely-sensed observations

Jeremiah J. Nieves[1, 2], Alessandro Sorichetta[1], Catherine Linard [3], Maksym Bondarenko[1], Jessica E. Steele[1], Forrest R. Stevens [4], Andrea E. Gaughan [4], Alessandra Carioli [1], Donna Clarke [1], Thomas Esch [5], & Andrew J. Tatem [1, 6]

1. WorldPop, Dept. of Geography and Environmental Science, University of Southampton, Southampton, UK
2. Economic and Social Research Council South Coast Doctoral Partnership, UK
3. Dept. of Geography, Univesite de Namur, Namur, Belgium
4. Dept. of Geography and Geosciences, University of Louisville, Louisville, KY, USA
5. German Aerospace Center (Deutsches Zentrum für Luft- und Raumfahrt; DLR), Munich, Germany
6. Flowminder Foundation, Stockholm, Sweden

ABSTRACT

Mapping settlement extents at the annual time step has a wide variety of applications in demography, public health, sustainable development, and many other fields. Recently, while more multitemporal urban feature or human settlement datasets have become available, issues still exist in remotely-sensed imagery due to coverage, adverse atmospheric conditions, and expenses involved in producing such feature sets. These challenges make it difficult to increase temporal coverage while maintaining high fidelity in the spatial resolution. Here we demonstrate an interpolative and flexible modeling framework for producing annual built-settlement extents. We use a combined technique of random forest and spatio-temporal dasymetric modeling with open source subnational data to produce annual 100m x 100m resolution binary settlement maps in four test countries of varying environmental and developmental contexts for test periods of five-year gaps. We find that in the majority of years, across all study areas, the model correctly identified between 85-99% of pixels that transition to built-settlement. Additionally, with few exceptions, the model substantially out performed a model that gave every pixel equal chance of transitioning to the category “built” in each year. This modelling framework shows strong promise for filling gaps in cross-sectional urban feature datasets derived from remotely-sensed imagery, provide a base upon which to create future built/settlement extent projections, and further explore the relationships between built area and population dynamics.

Keywords
Built, urban growth, random forest, dasymetric, population,

 doi:10.20944/preprints201812.0250.v1

ACKNOWLEDGEMENTS

JJN is funded through the Economic and Social Research Council's Doctoral Training Program, specifically under the South Coast branch (ESRC SC DTP). Feedback/support of early versions of the modelling framework from Dave Martin (University of Southampton), and Deborah Balk (City University of New York) was influential and much appreciated on the final product presented here. Many of the spatial covariates used here are the product of the "Global High Resolution Population Denominators Project" funded by the Bill and Melinda Gates Foundation (OPP1134076) (doi:10.5258/SOTON/WP00644). The authors acknowledge the use of the IRIDIS High Performance Computing Facility, and associated support services at the University of Southampton, in the completion of this work.

AUTHOR CONTRIBUTIONS

JJN, AS, JES, and AJT designed research. FRS, AEG, CL and JJN contributed to previous model concepts that resulted in the presented model realization. DC and AC contributed significant knowledge transfer on bootstrapping and growth curves. JJN carried out analyses and research. JJN, MB, and TE provided data and or carried out data pre-processing. JJN wrote the modelling script with MB providing the code framework for the larger scale data production. JJN wrote the manuscript with contributions and edits from all other authors.

 doi:10.20944/preprints201812.0250.v1

1. INTRODUCTION

Many countries define urban as a function of some population density, economic functional area, or based upon administrative jurisdictions (United Nations, 2015), but this is not conducive to applications requiring global consistency in definitions (Potere & Schneider, 2007). As a result, many studies have turned to a definition based upon the remotely sensed physical features of urban areas, i.e. the built environment, but even this can vary across space and time due to materials used, differences in urban morphology, and the surrounding environmental context (A Schneider, Friedl, & Potere, 2010; Annemarie Schneider & Woodcock, 2008; Small, 2009). Initially, remotely sensed urban definitions were optically-based thematic classifications of land cover, typically captured the "built-environment," including buildings, roads, runways, and, sometimes erroneously, bare soil (Bartholomé & Belward, 2005; Potere, Schneider, Angel, & Civco, 2009; A Schneider et al., 2010; Annemarie Schneider, Friedl, McIver, & Woodcock, 2003). Later improvements using supporting information about the surrounding environment and vegetation during post-processing helped discern the true built environment from the surrounding land covers (A Schneider et al., 2010). Coinciding with advances in imagery, statistical methods, and computational resource availability, several high-resolution global datasets have combined optical imagery at various resolutions and utilized Synthetic Aperture Radar (SAR) data to refine the capture of urban features with a focus on vertical human-made structures (T Esch et al., 2013; Pesaresi et al., 2013, 2016). However, it remains a challenge to produce a consistent product while maintaining high temporal and spatial fidelity meaning most of the multi-temporal urban feature data sets are cross-sectional across a larger period. Further, the resource cost of producing these data remains relatively high and there can be pre-existing gaps in the data, due to selected sensor/platform characteristics or problems and adverse atmospheric conditions, prior to the other fidelity considerations.

One way to address these issues is to leverage years where remotely-sensed urban feature extractions with high spatial fidelity and interpolate for missing time points and areas of interest is modelling between and/or beyond the coverage of remotely sensed data. Overall, urban feature/built growth models have disproportionately focused on high-income countries, which have different urban feature/built dynamics than low- and middle-income countries (Angel, Sheppard, & Civco, 2005; Linard, Tatem, & Gilbert, 2013; Seto, Fragkias, Guneralp, & Reilly, 2011; United Nations, 2015), and most have been limited to city or regionally specific models (Barredo, Demicheli, Lavalle, Kasanko, & McCormick, 2004; Batty & Xie, 1994; Clarke & Gaydos, 1998; Clarke, Hoppen, & Gaydos, 1997; Leao, Bishop, & Evans, 2004; Linard et al., 2013; Sante, Garcia, Miranda, & Crecente, 2010; White & Engelen, 1997, 2000). Previous methods of modelling urban land use and built land cover growth across space and time at the continental and global scales include land cover/land use transition models (Tayyebi et al., 2013; Verburg, Schot, Dijst, & Veldkamp, 2004) and cellular automata models (Batty, 2009; Sante et al., 2010; Verburg et al., 2002), with features or thematic classes extracted from remotely sensed imagery being the primary source of cross-sectional input for these models (T Esch et al., 2013; Patel et al., 2015; Pesaresi et al., 2013, 2016; A Schneider et al., 2010). Of the few models predicting urban feature growth across the globe with a standardized framework, almost none have explicit spatial prediction finer than country level summaries (Angel, Parent, Civco, Blei, & Potere, 2011; Seto et al.,

 doi:10.20944/preprints201812.0250.v1

2011). Models that do provide discrete spatial predictions, do not allow local sub-national variation to drive the modelled changes or have not been assessed against comparable existing datasets (Angel et al., 2011; Goldewijk, Beusen, & Janssen, 2010; Linard et al., 2013; Seto, Guneralp, & Hutyra, 2012).

Having time series of regular observations of built settlement extents and their corresponding populations are significant given that forecasted growth of populations within dense urban areas are expected to continue through 2050, and much of that increase will occur within Africa and Asia (Angel et al., 2005; United Nations, 2015). Rapidly changing magnitudes and distributions of both settlements and populations have significant implications for sustainability (B. Cohen, 2006), climate change (McGranahan, Balk, & Anderson, 2007; Stephenson, Newman, & Mayhew, 2010), and public health (Chongsuvivatwong et al., 2011; Dhingra et al., 2016), amongst others. At local and regional levels, the availability, or non-availability, and accuracy of built and settlement extent type data affect measured population distributions, densities, and built type, e.g. urban, peri-urban, and rural, that then inform and shape policies. The 2030 Sustainable Development Goals (SDGs), which have a focus on accounting for and including "all people everywhere", have reinforced this need for readily and globally available baseline data to guide efforts to meet development goals (United Nations, 2016). Further, outputs of a good model of time-specific urban/built growth can be used to guide training selection or post-processing of future remotely-sensed urban feature datasets.

In this study, urbanization, or urban transition, is taken within a remote sensing context to be the physical transition of land cover from non-built-settlement, e.g. natural land cover, to built-settlement. We hereafter refer to areas that are comprised of habitable vertical structures and their immediate non-natural surroundings as "built-settlement" or BS. With this definition in mind, we leveraged recent advances in multi-temporal global BS feature datasets, global environmental datasets, subnational census-based population data, and computational methods to develop a globally applicable and flexible modelling framework. Our specific objectives were to i) determine if random forests can reasonably predict non-BS to BS transitions, ii) using random forests, create an automated globally applicable framework that can produce spatially explicit estimates of BS extent at annual steps using sub-nationally driven covariates and total population counts, iii) validate the model performance by an annual BS dataset and comparing the model predictions to the "observed" data.

2. METHODS AND DATA

2.1 Study Areas and Data

We selected four low-, middle-, and high-income countries from across the globe to capture a variety of BS morphologies, contexts, and evolutions as well as to demonstrate the flexibility of the model for various regions. The countries selected here were Panama, Switzerland, Uganda, and Vietnam. We also selected a "best-performance scenario" set of covariates, partly informed by the findings of an Africa-specific growth model by Linard et al. (2013), to give immediate environmental/land cover context and connectivity of areas to urban/built agglomerations. Ultimately, the model is not dependent on any specific covariates, retaining a level of flexibility for use in a wide variety of applications. For

Preprints (www.preprints.org) | NOT PEER-REVIEWED | Posted: 20 December 2018 doi:10.20944/preprints201812.0250.v1

example, we have also tested the model using a minimal set of globally available predictive covariates to provide input to other modelling efforts and avoid circular inference by end users. In the case presented here, chosen covariates were either time-specific or assumed to be temporally invariant (Table 1). All covariates were pre-processed, resampled to 3 arc second (~100m at the Equator) based on data type, and co-registered. All data used to restrict the area of modelling and inform the redistribution of transitions are also detailed in Table 1. Further details on pre-processing of specific covariates are provided in the Supplemental Material.

Table 1. Covariates used for predicting the probability of transition or in the model's transition re-distribution process.

Covariate	Variable Name(s) in Random Forest	Description	Use	Time Point(s)	Original Spatial Resolution(s)	Data Source(s)
Built-settlement	esa_cls190	Binary BS extents	Predictive, Restrictive, Redistributive	2000 2005 2010 2015	ESA 10 arc sec	(ESA CCI, 2017)
DTE Built-settlement	esa_cls190_dst_<*year*>	Distance to the nearest BS edge	Predictive	2000 2005 2010 2015	ESA 10 arc sec	(ESA CCI, 2017)
Proportion Built-settlement 1,5,10,15	esa_cls190_prp_<*radius*>_<*year*>	Proportion of pixels that are BS within 1,5,10, or 15 pixel radius	Predictive	2000 2005 2010 2015	ESA 10 arc sec	(ESA CCI, 2017)
Elevation	Topo	Elevation of terrain	Predictive		3 arc seconds	(Lehner, Verdin, & Jarvis, 2008)
Slope	Slope	Slope of terrain	Predictive		3 arc seconds	(Lehner et al., 2008)
DTE Protected Areas Level 1	wdpa_cat1_dst_2015	Distance to the nearest level 1 protected area edge	Predictive	2000, 2012	Vector	(U.N. Enviroment Programme World Conservation Monitoring Centre & IUCN World Commission on Protected Areas, 2015)
Water	---	Areas of water to restrict areas of model prediction	Restrictive		5 arc second	(Lamarche et al., 2017)
Subnational Population	---	Annual population by sub-national units	Predictive, Redistributive	2000 - 2020, annually	Vector	(Doxsey-Whitfield et al., 2015)
Weighted Lights-at-Night (LAN)	----	Annual lagged and sub-national unit normalised LAN	Redistributive	2000-2016, annually	30 arc second (2000-2011) 15 arc second (2012-2016)	DMSP (WorldPop, Department of Geography and Geosciences, Département de Géographie, & Center for International Earth Science Information Network (CIESIN), 2018; Zhang, Pandey, & Seto, 2016) VIIRS(Earth Observation Group NOAA National Geophysical Data Center, 2016; WorldPop et al., 2018)
Travel Time 50k	tt50k	Travel time to the nearest city centre containing at least 50,000 people	Predictive	2000	30 arc second	(Nelson, 2008)
Urban Accessibility 2015	urbanaccessibility_2015	Travel time to the nearest city edge	Predictive	2015	30 arc second	(Weiss et al., 2018)
ESA CCI Land Cover (LC) Class [a]	ccilc_dst<*class number*>_<*year*>	Distance to nearest edge of individual land cover classes	Predictive	2000	10 arc second	(ESA CCI, 2017)
Distance to OpenStreet Map (OSM) Rivers	osmriv_dst	Distance to nearest OSM river feature	Predictive	2017	Vector	(OpenStreetMap Contributers, 2017)

Preprints (www.preprints.org) | NOT PEER-REVIEWED | Posted: 20 December 2018 doi:10.20944/preprints201812.0250.v1

Distance to OpenStreet Map (OSM) Roads	osmroa_dst	Distance to nearest OSM road feature	Predictive	2017	Vector	(OpenStreetMap Contributers, 2017)
Average Precipitation	wclin_prec	Mean Precipitation, 1950-2000	Predictive	Single	30 arc sec	(Hijmans, Cameron, Parra, Jones, & Jarvis, 2005)
Average Temperature	wclim_temp	Mean temperature, 1950-2000	Predictive	Single	30 arc sec	(Hijmans et al., 2005)

a Some classes were collapsed: 10-30 → 11; 40-120 → 40; 150-153 → 150; 160-180 → 160

2.1.1. Built-Settlement Data

We chose to use the "Urban" thematic class, class 190, from the annual ESA CCI landcover dataset, hereafter ESA, for our study because of its annual coverage from 1992 to 2015, allowing for the exclusion of years in the modelling process for validation of outputs. For our period of interest, 2000 to 2015, the ESA data creates annual 10 arc sec resolution (~300m at Equator) datasets by looking for thematic class changes from a baseline land cover map, produced using MERIS imagery, using 30 arc second (~1 km at the Equator) SPOT VGT imagery (1999-2013) and PROBA-V imagery (2014-2015) (UCL Geomatics, 2017). Starting in 2004, if there are changes detected, then the individual pixels of change detected at 30 arc second are further delineated using 10 arc second MERIS or PROBA-V imagery (UCL Geomatics, 2017). To reduce false detections, changes must be observed over two years or more (UCL Geomatics, 2017). Furthermore, the Global Human Settlement Layer (GHSL) (Pesaresi et al., 2013, 2016) and Global Urban Footprint (GUF) (T Esch et al., 2013) datasets are utilized in defining the extents of the ESA Urban class (UCL Geomatics, 2017). While still undergoing full validation, initial validation efforts estimate the 2015 Urban class user and producer accuracies between 86-88 percent and 51-60 percent, respectively (UCL Geomatics, 2017). We also test and validate a single year from an alpha version of forthcoming multi-temporal World Settlement Footprint (WSF) dataset, known as WSF Evolution (Thomas Esch et al., 2018), and present the results in the Supplementary Material.

Table 2. Summary of built-settlement transition data by country and period. Areal units here are pixels (~100m) as that is the unit handled by the model which looks at relative areal changes as opposed to absolute areal changes.

Country	Period	Initial Non-Built Area (pixels)	Observed Transitions
Panama	2000-2005	8,901,004	0.03 %
	2005-2010	8,898,679	0.09 %
	2010-2015	8,890,339	0.75 %
Switzerland	2000-2005	6,816,510	1.56 %
	2005-2010	6,710,069	0.08 %
	2010-2015	6,704,973	0.01 %
Uganda	2000-2005	28,231,555	0.07 %
	2005-2010	28,210,425	0.04 %
	2010-2015	28,200,084	0.04 %
Vietnam	2000-2005	40,108,425	0.11 %
	2005-2010	40,063,545	0.18 %
	2010-2015	39,990,858	0.38 %

2.1.2 Population Data

Annual population estimates from 2000 to 2020 for subnational areas were provided by Center for International Earth Science Information Network (CIESIN) in tabular format with unique IDs corresponding to a globally consistent grid containing the unique subnational

Preprints (www.preprints.org) | NOT PEER-REVIEWED | Posted: 20 December 2018 doi:10.20944/preprints201812.0250.v1

unit IDs and harmonized coastlines(Doxsey-Whitfield et al., 2015). Populations and their corresponding areas are based upon the Gridded Population of the World (GPW), version 4 and as such follow the methods detailed in Doxsey-Whitfield et al. (2015) for the interpolation of population between years of official counts or estimates.

2.2 Built-Settlement Growth Model (BSGM)

2.2.1 Overview

Here we interpolated for every year between a set of timepoints, $T = \{t0, t_1, t_2, \ldots, t1\}$ where *t0* is the initial observed timepoint, *t1* is the final observed timepoint, and all other times *t* are points lying between *t0* and *t1* for which we had observed BS extents. The time between any two observed time points *t* is referred to as a period, *p*. Within this study, *t0* is 2000, *t1* is 2015, and we also have observed time points at 2005 and 2010, however the framework can handle any regularly spaced intra-period time-step if the input data corresponds. Therefore, in this study, for the ESA informed models we are carrying out modelling on three time periods, 2000-2005, 2005-2010, 2010-2015, for a total of 12 years interpolated. We generalize the process to determine the timing and number of transitions for each time step independently for each subnational unit, hereafter unit, as follows:

1. Create a population map for all $t_{observed}$ in *T*.
2. At all $t_{observed}$, for each unit, extract the time-specific population count within the time specific BS extents and derive the corresponding average BS population density.
3. On a unit-by-unit basis, interpolate the extracted BS population count between each $t_{observed}$ using piecewise-fit logistic growth curves and BS population density by fitting natural cubic splines across all $t_{observed}$.
4. Estimate expected unit, time-step-specific, total BS extent area, in number of pixels, and the expected number of transitions for that time-step based upon predicted unit-specific total BS population and BS population density.
5. For every unit, adjust the expected transitions by the sum of all expected transitions across the given period, t_a and t_b, e.g. 2000-2005 or 2005-2010, and divide by the total observed changes, e.g. 2005 BS extents minus 2000 BS extents. Repeat for all periods.
6. For each unit, use the adjusted predicted transitions from step five as relative weights within a given unit to dasymetrically redistribute observed transitions from the larger source period to smaller individual time-steps, i.e. years, while maintaining the original number of transitions when all time-steps are summed. Repeat for all periods.

To spatially disaggregate the predicted transitions, we first train a Random Forest (RF) model (Breiman, 2001) to produce a continuous surface representing the probability of a given grid pixel transitioning from non-BS to BS between *t0* and *t1*. For every time-step, processing each subnational unit independently, we utilized unit normalized lagged lights-at-night (LAN) data to annually adjust the base RF-derived transition probabilities. The assumption behind this being that areas that underwent the largest increase in brightness, relative to the rest of the unit in a single time-step, have a higher probability of transitioning and vice versa. From the pixels that were known to have transitioned, as indicated in the input

Preprints (www.preprints.org) | NOT PEER-REVIEWED | Posted: 20 December 2018 doi:10.20944/preprints201812.0250.v1

BS data, we selected pixels with the n^{th} highest probabilities for transition, where n was equal to the number of pixels predicted to transition for that time-step. We then converted those pixels to BS, recorded the new BS extents, and used those extents as the basis for the next time-step of transitions. This resulted in a series of regularly spaced time-specific binary spatial predictions of the BS extents in raster format. A full process diagram is shown in Figure 1. All modelling and analyses were carried out using R 3.4.2 (R Core Team, 2016) on the IRIDIS 4 high-performance computing cluster (see Supplemental Material for code).

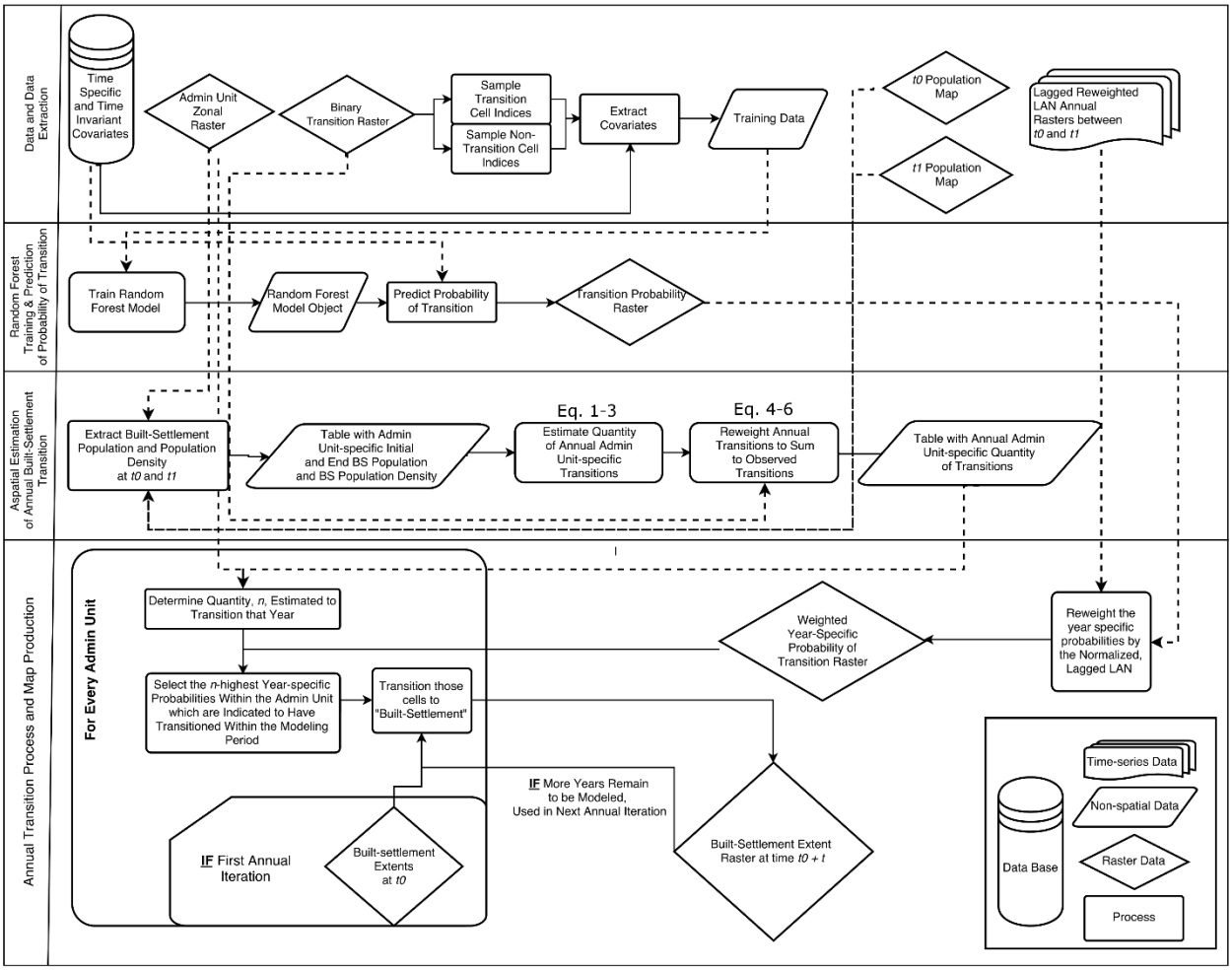

Figure 1. Overview of the generalized modelling process for a case of only two observed timepoints, *t0* and *t1*, with references to utilized equations.

2.2.2 Random Forest (RF) Estimation of the Probability of Transition

Given that the binary dataset of transition/non-transition constitutes an intrinsic "imbalanced set" (He & Garcia, 2009), i.e. there are many more non-transitions than transitions; we adopted a stratified random over/under-sampling method (He & Garcia, 2009), similar to (Linard et al., 2013), as follows: (i) randomly sample 80 percent of the pixels that transitioned, up to 50,000 and, (ii) randomly sample an equal number of pixels that did not undergo transition. The choice for equal sampling of each stratum was determined by testing different relative proportions and samples sizes until finding the most consistent and best model results, balancing performance and efficiency.

Preprints (www.preprints.org) | NOT PEER-REVIEWED | Posted: 20 December 2018 doi:10.20944/preprints201812.0250.v1

To create a probability of transition surface for the complex and non-linear phenomenon of BS transition, we utilized a RF model to accurately and efficiently model across an entire country at the pixel (3 arc second) level in an automatable and parallelizable fashion. We trained the classification RF on whether a pixel had transitioned between time *t0* and *t1* (1) or not transitioned (0) against the corresponding values of covariates at time *t0*. We used the constructed RF to predict for the entire given country. Rather than accepting the default output of the RF classifier, which outputs a single predicted class as indicated by the majority of the predictions of its individual constituent trees, we wanted a continuous, 0.00 to 1.00, probability of transitioning in to discriminate between high and low probabilities. Given that we trained the RF as a binary classifier, we took the mean of the individual tree predictions for each pixel. This class probability has a value between 0.00 and 1.00 represents the posterior probability of a pixel being classified by the RF as transitioning between *t0* and *t1* (Breiman, 2001).

2.2.3 Population Mapping of Endpoints

To interpolate, we first needed a spatially-explicit best estimate of the subnational unit specific BS population at all observed timepoints in the modelling period. To get this we created a population surface using the available time-specific and, assumed, time-invariant covariates (see Supplemental Material, Table A2) using the WorldPop RF method, described in Gaughan et al. (Gaughan, Stevens, Linard, Jia, & Tatem, 2013) and Stevens et al. (Stevens, Gaughan, Linard, & Tatem, 2015), to dasymetrically redistribute the time-specific population totals from the subnational unit level to 3 arc second grid pixels (Mennis, 2003; Mennis & Hultgren, 2006; 2015).

For any given time point in the population modelling, we included the distance to nearest BS edge for the *t0* timepoint, i.e. 2000, as population relates to older parts of a BS agglomeration differently from newer ones (2016). For example, if we were to model the population map of 2010 we would include the distance to nearest BS edge for 2010 as one of the predictive covariates as well as the distance to nearest BS edge corresponding to the 2000 BS extents. This was done to avoid centres of agglomerations being assigned artificially low population densities relative to the preceding modelled time point (2016). We then extracted and summed by unit the total populations that were spatially coincident with the BS extents and derived the corresponding BS population density for use in the BSGM predictive phases.

2.2.4 Transition Magnitude Estimation

To estimate the number of transitions for each time-step within the study period, we used the predicted BS population changes and the predicted changes in BS population density for every unit. We first interpolated the BS population count of each unit *i* for every year, BSPOP(t), by fitting logistic growth curves (Booth, 2006), in a piecewise manner, i.e. for each time-period between observed points, using the year-specific total population, $K_i(t)$, as the varying carrying capacity (Meyer & Ausubel, 1999) as shown in Equation 1

$$BSPOP_i(t) = K_i(t) * \frac{e^{r_i * t + C_i}}{1 + e^{r_i * t + C_i}} \quad \text{[Eq. 1]}$$

where *t* is the number of time steps from the given period's origin, e.g. for period 2000-2005 2002 corresponds to $t = 2$, and r_i and C_i are determined by fitting a least-squares linear

Preprints (www.preprints.org) | NOT PEER-REVIEWED | Posted: 20 December 2018 doi:10.20944/preprints201812.0250.v1

regression to the set of observed values after having been transformed via Equation 2.

$$\ln\left(\frac{BSPOP_{it_{observed}}}{K_{it_{observed}} - BSPOP_{it_{observed}}}\right) \quad \text{[Eq. 2]}$$

We then interpolated the unit average BS population density across all observed time points in the study period using natural cubic splines (McNeil, Trussell, & Turner, 1977) and the observed points as the knots, i.e. for ESA 2000, 2005, 2010, and 2015. The overriding theory behind selecting logistic growth curves and the cubic splines for interpolating comes from the sigmoid shape of these curves. That is, BS population and population density are assumed to follow the s-shaped curve by having low growth/decay rate in the beginning, a period of rapid change after a certain point, and then a slowing growth/decay rate as various constraints or carrying capacities, e.g. demographic, environmental, economic, affect the population (J. E. Cohen, 1995; Sibly, 2005).

Using the interpolated unit BS population and the interpolated unit-average BS population density, we simply relate population and population density to produce areal units, in our case pixels, to get the expected number of transitions in Equation 3

$$BSCNT_i(t) = \frac{BSPOP_i(t)}{BSD_i(t)} \quad \text{[Eq. 3]}$$

where $BSD_i(t)$ is the unit, i, average BS population density at time t. See Supplemental Materials for how predicted "negative growth" resulting from Equations 1-3 was handled.

2.2.5Dasymetric Redistribution of Transitions Across Time

The number of predicted transitions derived from Equations 1-3 are not inherently constrained by the observed transitions between any two observed time points. To match the total number of observed transitions for the modelled period, we reweighted the transitions of each time-step on a unit-by-unit basis. This is essentially a temporal dasymetric redistribution of transitions from the larger source period, e.g. 2000-2005, to the smaller target periods of t, e.g. 2001,2002, etc., based upon temporal information contained in the time-specific unit population totals. To calculate the weight for each time-step, w_t, we write the calculation in Equation 4 as:

$$w_{t_i} = \frac{\widehat{BSCNT_i}(t)}{\sum_1^k \widehat{BSCNT_i}(t)} \quad \text{[Eq. 4]}$$

where t is again relative to the given period from 1 to the last year k and all w_t for a given unit i sum to one. To obtain the temporally weighted transitions, $\widehat{BSCNT}_{it}$, we multiplied the weight of each year by the observed number of transitions in Equation 5, rounding to the nearest whole number for each year (see Supplemental Materials, section A4 for obtaining agreement with rounding differences).

Preprints (www.preprints.org) | NOT PEER-REVIEWED | Posted: 20 December 2018 doi:10.20944/preprints201812.0250.v1

$$\widehat{BSCNT}_{ti} = round(w_{ti} * \Delta BSCNT_i) \quad \text{[Eq. 5]}$$

Where $\Delta BSCNT_i$ is the number of observed transitions, in pixels, from non-BS to BS for a given unit *i*. This allows the model to maintain agreement of transitions between the points that we interpolated.

2.2.6 Spatially Disaggregating Transitions Using Annual Unit-specific LAN-weights

For each period, we then processed the tabular predicted transitions into time-specific BS extent maps, i.e. spatially allocated the transitions within each subnational unit for each time-step. We spatially assigned the transitions within each unit using the RF-derived transition probability surface adjusted by time-specific weights in the form of subnational unit normalized LAN brightness differences, i.e. one time-step lags (see Supplemental Material). Given that the non-BS to BS, or "BS growth," transition process is iterative in nature, we began by taking the extents of the previous time-step, or the previous observed extents if *t* was equal to one. We limited the location(s) where transitions could be allocated within the subnational unit to pixels where transitions were observed to have occurred, as defined by the input BS data. For every one of those locations, *j*, assuming they weren't transitioned in previous steps, we retrieved the transition probability as calculated in the transition probability surface. We took this base probability of transition for every pixel *j* and adjusted it by the spatially coincident lagged and weighted LAN data, for time-step *t*, using Equation 6:

$$P_{adj}(transition)_{ijt} = wLAN_{ijt} * P(transition)_{ij} \quad \text{[Eq. 6]}$$

where $P(transition)_{ij}$ is the RF-derived transition probability where transition was observed, $wLAN_{ijt}$ is the corresponding adjusted LAN difference observed for the time-step *t*, and $P_{adj}(transition)_{ijt}$ is the adjusted probability of transition for the time-step *t* in a given pixel *j* within the administrative unit *i*. Similar to previous models (Linard et al., 2013; Tayyebi et al., 2013), we assumed pixels with a higher probability of transition are more likely to transition before pixels with lower probabilities. We selected the n^{th} highest probabilities from the subset of potential transition pixels, where *n* was equal to $\widehat{BSCNT}_{ti}$, changed the value of those selected pixels to represent a transition to BS, and output the union of the new transitions and previous BS extents as the predicted BS extents for that time-step. We repeated this procedure using the newly produced extents for the preceding time-step as the base BS extent for the next time-step's transition procedure, until all time-steps for the period were processed and then the entire procedure was repeated until all periods had been processed.

2.3 Analyses

2.3.1 Validation and Comparison Metrics

While the RF produces its own validation estimates (Breiman, 2001), we tested the accuracy of the RF classifier by randomly sampling 100,000 pixels, not utilized in the

Preprints (www.preprints.org) | NOT PEER-REVIEWED | Posted: 20 December 2018 doi:10.20944/preprints201812.0250.v1

training of the RF, for validation. We selected this sample size as we were able to obtain sample prevalence rates equal to the known true prevalence rates of each country while still maintaining efficiency. Based on this sample, we plotted receiver operator curves (ROCs) and, given the imbalanced data (Haibo He & Garcia, 2009; Saito & Rehmsmeier, 2015), precision recall curves (PRCs) with simulated perfect and random classifier curves for comparison.

Here, for the ESA models, we are comparing the predicted extents to all withheld extents between 2000 and 2015. For every year of prediction, we determined whether a pixel was True Positive, False Positive, False Negative, or True Negative, TP, FP, FN, TN, respectively. We calculated contingency table-based metrics to evaluate classification accuracy based primarily on the F_1 score (Table 3) which is the harmonic mean of recall and precision, the quantity disagreement (Pontius & Millones, 2011), and the allocation disagreement (Pontius & Millones, 2011). We aggregated the pixel level results, to the unit level and calculated the same metrics since precision, and by extension F_1, is sensitive to the corresponding prevalence and is subject to the modifiable areal unit problem (MAUP) (Openshaw, 1984).The MAUP not only reduces variance in value distributions the more the data are aggregated from their original resolution (Openshaw, 1984), but will result in different prevalences with different subnational area, i.e. zonal, configurations. The equations of the metrics calculated are listed in Table 3.

Table 3. Classification agreement metrics utilized and a brief description of each. The F1-score is interpreted as the harmonic mean of precision and recall. TP is "True Positive", FP is "False Positive", FN is "False Negative", and TN is "True Negative."

Metric	Equation	Range and Interpretation
Recall (Sensitivity) (Rogan & Gladen, 1978)	$\frac{TP}{TP+FN}$	0 (no recall) – 1 (perfect recall)
Specificity (Rogan & Gladen, 1978)	$\frac{TN}{FP+TN}$	0 (no specificity) – 1 (perfect specificity)
Quantity Disagreement (Pontius & Millones, 2011)	$\frac{\left\lvert\frac{FN-FP}{TP+FP+FN+TN}\right\rvert + \left\lvert\frac{FP-FN}{TP+FP+FN+TN}\right\rvert}{2}$	0 (no disagreement) – 1 (complete disagreement)
Allocation Disagreement (Pontius & Millones, 2011)	$2 * \min\left(\frac{FP}{TP+FP+FN+TN}, \frac{FN}{TP+FP+FN+TN}\right)$	0 (no disagreement) – 1 (complete disagreement)
F_1 score	$\frac{2 * \frac{TP}{TP+FP} * \frac{TP}{TP+FN}}{\frac{TP}{TP+FP} + \frac{TP}{TP+FN}}$	0 (worst) – 1 (best)

Additionally, to assess whether the modelling is worth the effort, we constructed a null model that randomly assigns the transitions to a year within the given period, with every year having an equal likelihood, and carried out predictions for each year within pixels that were known to have transitioned for comparability with our model. Again, we determined for each pixel whether it was a TP, FP, FN, or TN and calculated metrics to compare the BSGM and the null model at the across each country at the pixel level, and at the unit level. The null model

Preprints (www.preprints.org) | NOT PEER-REVIEWED | Posted: 20 December 2018 doi:10.20944/preprints201812.0250.v1

was bootstrapped 500 times based upon resource limits and prediction stability, for each year and was specific to each country.

3. RESULTS

Across all study areas, two-thirds of the modelled years correctly predicted between 85-99 percent of transition pixels. For all years, again at the pixel level, the BSGM displayed low quantity and allocation disagreement in both absolute and relative terms. Similarly, the pixel level F1 score, with few exceptions, was higher than the null model, yet had more variance in absolute terms of performance. Comparable results were found at the unit level, with particularly good results in the middle and later years of the study period.

3.1 RF Performance

The ROC plots in Figure 2 show that the RFs approach the performance of the theoretical perfect model. However, given the imbalanced data, the PRC plots (Figure 2) show a more nuanced picture of performance where a maximum level of precision is quickly achieved, remains steady up to a certain value of recall that varies by study area, and then precision quickly decreases with increasing recall.

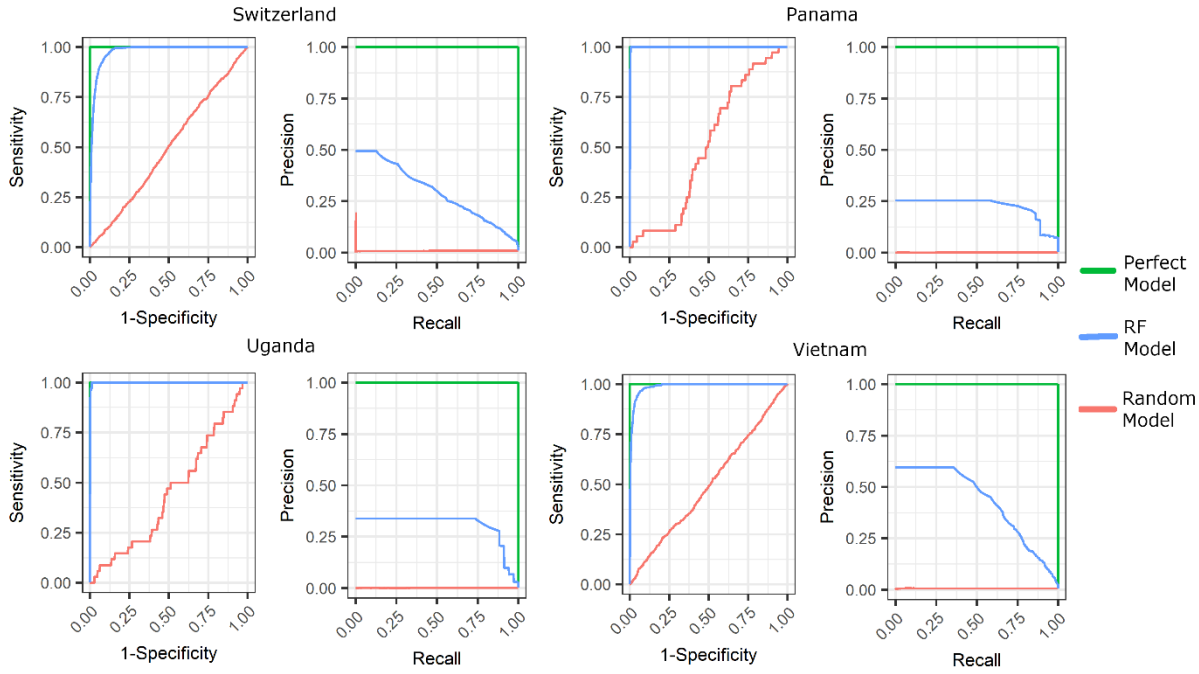

Figure 2. Receiver Operator Curve (left plots) and Precision Recall Curves (right plots) with the RF model performance, blue lines, against a random model, red lines, and a perfect model, green lines, for each modelled country and input dataset.

Of the covariates informing the RFs of the models, we consistently saw that the most important predictors of a pixel transitioning from non-BS to BS were covariates related to distance ("esa_cls190_dst_2000") and local density ("esa_cls190_prp_5_2000", "esa_cls190_prp_10_2000", and "esa_cls190_prp_15_2000") of BS established at the beginning of the overall study period, i.e. 2000, and connectivity of BS extents at the

Preprints (www.preprints.org) | NOT PEER-REVIEWED | Posted: 20 December 2018 doi:10.20944/preprints201812.0250.v1

beginning ("tt50k_2000") or end ("urbanaccessibility_2015" and "osmroa_dst") of the study period (Figure 3).

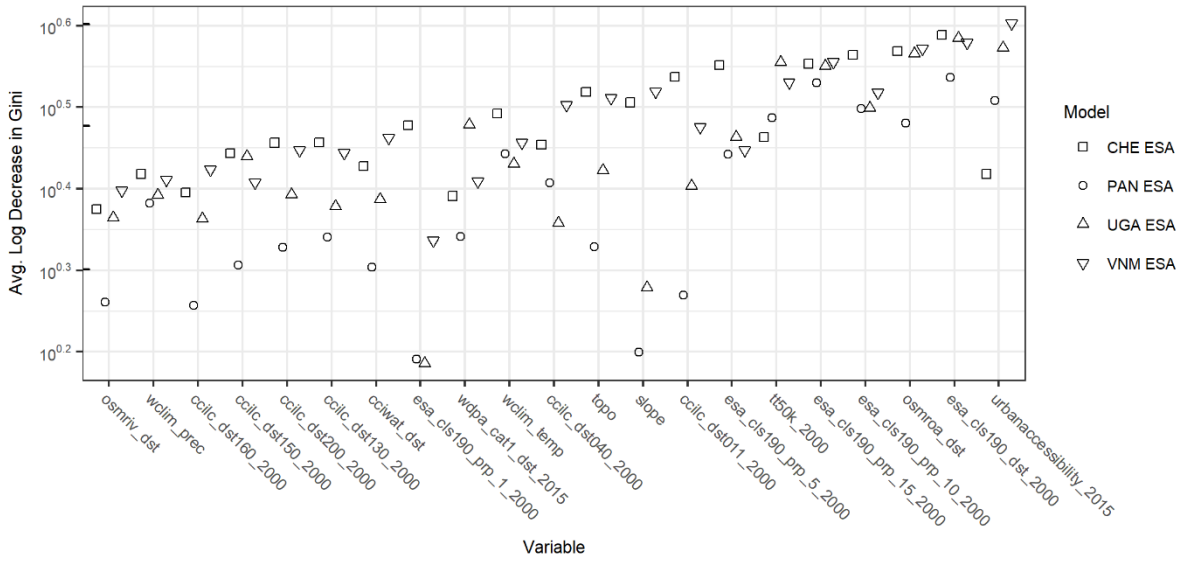

Figure 3. Random forest covariate importance as measured by the average log decrease in the Gini impurity when the covariate is used as the splitting criteria at nodes; higher values indicate better performance of covariate. Model for Swizerland (CHE) ESA, Panama (PAN) ESA, Uganda (UGA) ESA, and Vietnam (VNM) ESA, are shown. Refer to Table 1 for covariate names.

3.2 Pixel Level Results

Examining the proportion of pixels known to transition that were predicted correctly in Table 4, we show that out of 49 model years predicted, 33 of those years had correctly predicted proportions between 0.85 and 0.99. The ESA based modelled years ranged from 0.57 to 0.99 of pixels predicted correctly (Table 4). Note that one minus the proportion correct is equal to the total disagreement of the predicted pixels, i.e. the sum of the quantity and allocation disagreement (Pontius & Millones, 2011).

Table 4. Proportion of transition pixels predicted correctly by the BSGM by year. Note that 1 – the proportion correct is equal to the overall disagreement, i.e. the sum of the quantity and allocation disagreement.

Model	2001	2002	2003	2004	2006	2007	2008	2009	2011	2012	2013	2014
CHE ESA	0.718	0.573	0.628	0.975	0.987	0.979	0.975	0.983	0.999	0.998	0.997	0.997
PAN ESA	0.952	0.935	0.934	0.960	0.806	0.771	0.816	0.920	0.905	0.838	0.801	0.818
UGA ESA	0.814	0.787	0.803	0.929	0.912	0.877	0.877	0.909	0.940	0.893	0.865	0.878
VNM ESA	0.942	0.918	0.923	0.951	0.923	0.872	0.866	0.916	0.879	0.777	0.738	0.790

Examining the year-specific study area F1 scores in Figure 4, we show that the BSGM had low performance between 2001 to 2003, in absolute terms, and relatively near null model performance, across all ESA study areas. The F1 score for all modelled years after 2003 increases to quite good performance, with values approaching 1.0 in some cases, and the difference between the BSGM and null model performance increases even more dramatically (Figure 4).

Preprints (www.preprints.org) | NOT PEER-REVIEWED | Posted: 20 December 2018 doi:10.20944/preprints201812.0250.v1

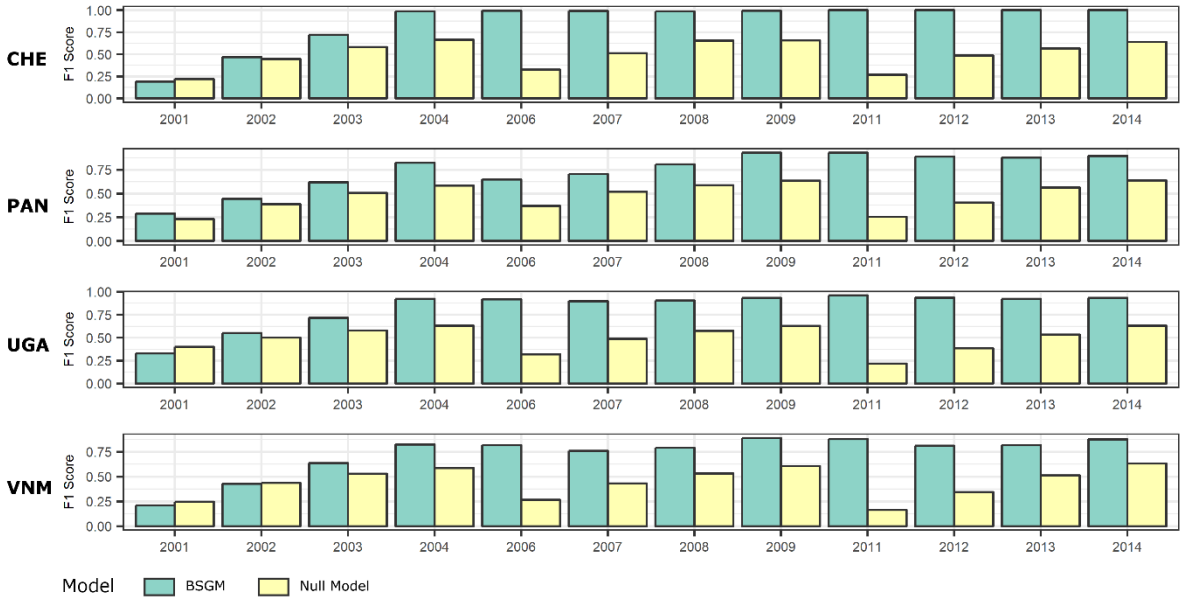

Figure 4. Pixel-level F_1 score by year for Switzerland (CHE), Panama (PAN), Uganda (UGA), and Vietnam (VNM) as compared to a null model. Full annual contingency data and metrics in supplementary material

Examining the source of the disagreement further, we display the observed quantity and allocation disagreement as well as the corresponding disagreements under the null model in Figure 5. We show that for all modelled years using the ESA data, the total disagreement is substantially less than that of the null model and predominantly, the disagreement produced by the BSGM model is predominantly due to allocation error (Figure 5). However, there does appear to be a pattern of increasing disagreement due to quantity error after 2010.

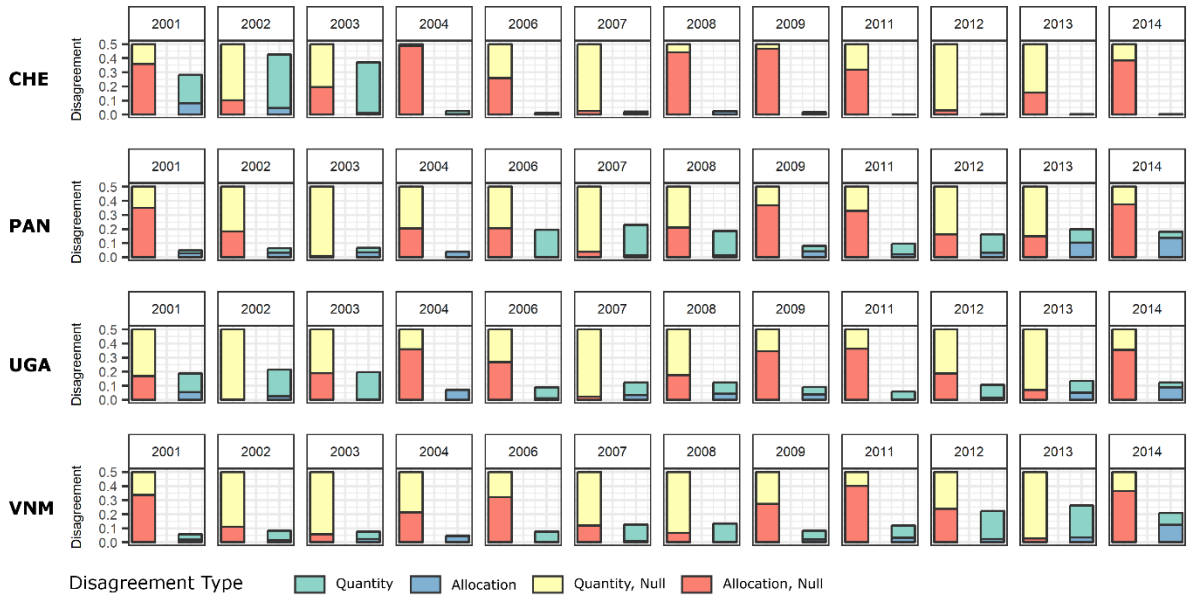

Figure 5. Pixel-level quantity and allocation disagreement of BSGM and null models for Switzerland (CHE), Panama (PAN), Uganda (UGA), and Vietnam (VNM) as compared to a null model, given in red. Full annual contingency data and metrics in supplementary material

Preprints (www.preprints.org) | NOT PEER-REVIEWED | Posted: 20 December 2018 doi:10.20944/preprints201812.0250.v1

3.3 Subnational Unit Level Results

Overall, at the unit level, we found results similar to the pixel-level results, including poor performance in absolute terms between 2001 to 2003, but some units were obviously performing worse than others as compared to the null model. Plotting the ESA-informed model distributions of unit-level F1 scores by study area and year against the corresponding null model performance, we show that the BSGM generally performs better in the majority of subnational units from which the transitions were disaggregated from (Figure 6). At worst, e.g. Vietnam 2002, approximately half of the units were still performing better than the null model (Figure 6). For quantity disagreement (Figure 7) and allocation disagreement (Figure 8), results similar to pixel level results were found.

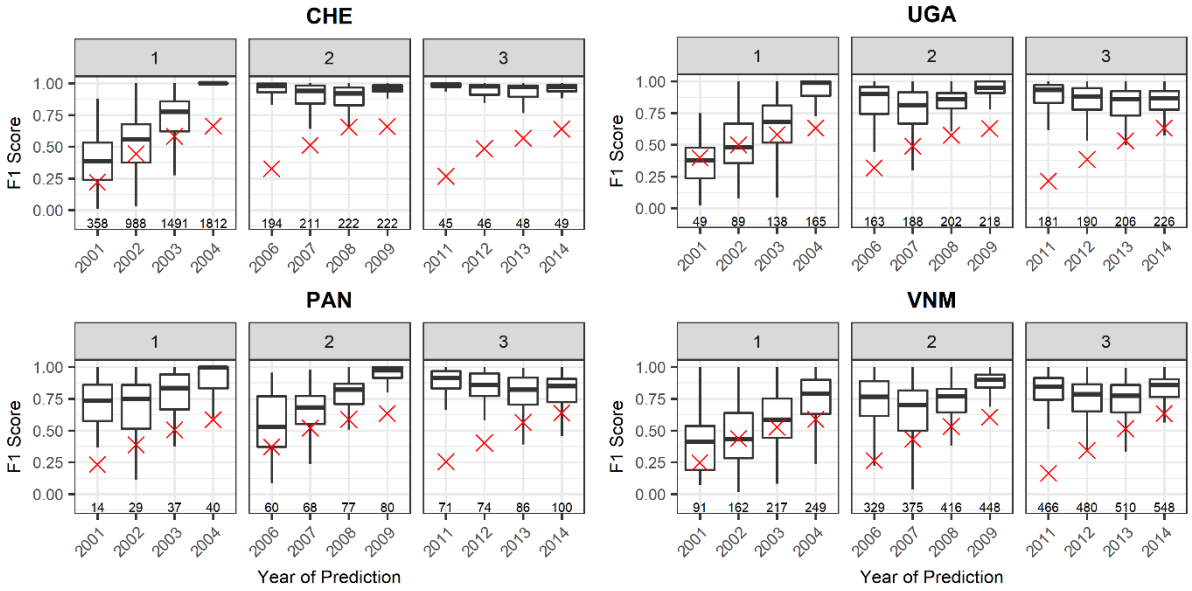

Figure 6. Unit level F_1 score box plots, by dasymetric period, of Switzerland (CHE), Panama (PAN), Uganda (UGA), and Vietnam (VNM) ESA informed models as compared to a null model, given by a red "x". Number of units exhibiting any transitions for each period and a defined metric value is given above the x-axis.

Preprints (www.preprints.org) | NOT PEER-REVIEWED | Posted: 20 December 2018 doi:10.20944/preprints201812.0250.v1

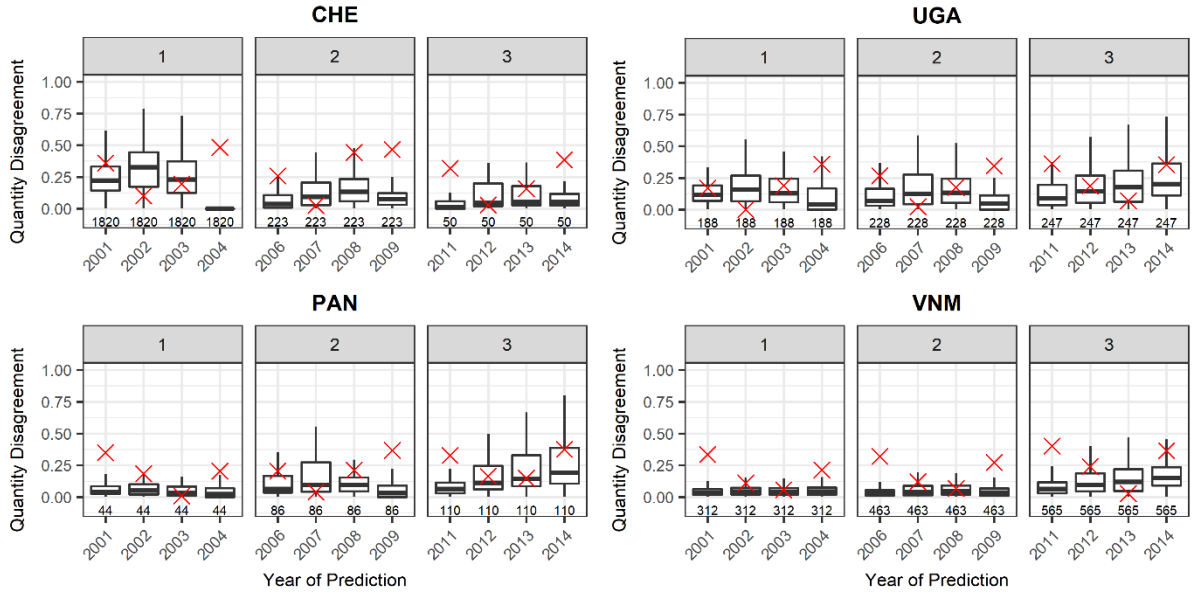

Figure 7. Unit level quantity disagreement box plots, by dasymetric period, of Switzerland (CHE), Panama (PAN), Uganda (UGA), and Vietnam (VNM) ESA informed models as compared to a null model, given by a red "x". Number of units exhibiting any transitions for each period and a defined metric value is given above the x-axis.

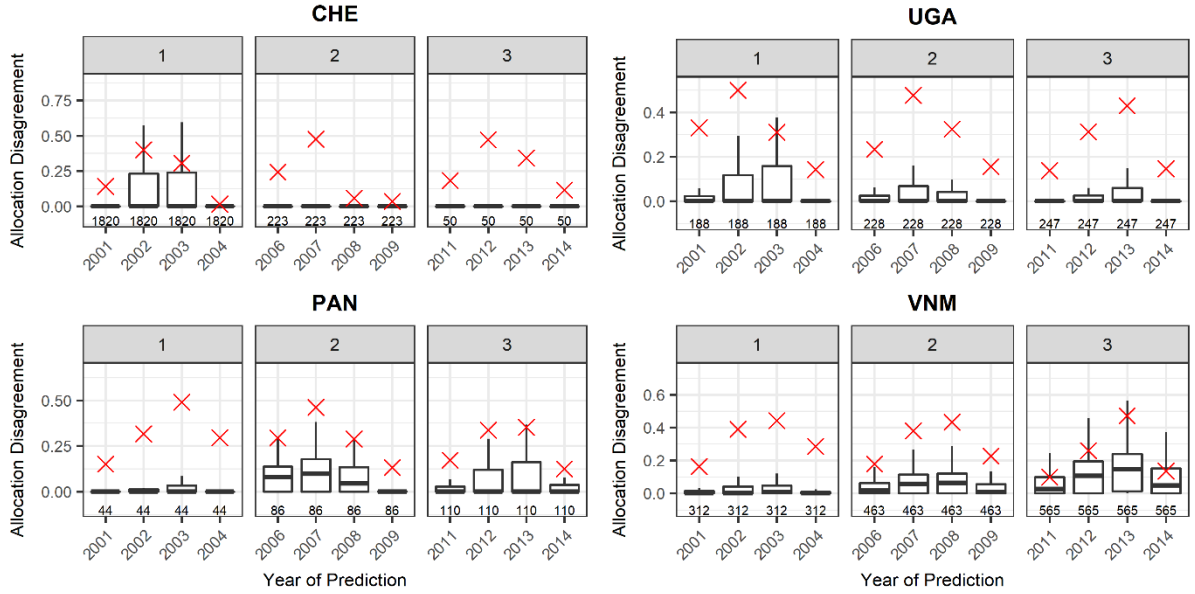

Figure 8. Unit level allocation disagreement box plots, by dasymetric period, of Switzerland (CHE), Panama (PAN), Uganda (UGA), and Vietnam (VNM) ESA informed models as compared to a null model, given by a red "x". Number of units exhibiting any transitions for each period and a defined metric value is given above the x-axis.

Plotting the unit-level metrics for all models as choropleth maps (see Supplementary Material for select maps and shape files containing contingency data), shows that years of generally good performance, the units of lesser performance are those that correspond to areas of less densely settled areas and the peripheries of established urban areas. Other years,

Preprints (www.preprints.org) | NOT PEER-REVIEWED | Posted: 20 December 2018 doi:10.20944/preprints201812.0250.v1

such as Uganda 2001, performed poorly across many units with no apparent pattern. Identical analyses for the WSF Evolution data are given in the supplementary materials as well.

4. DISCUSSION

The 2030 SDGs, have reinforced the importance of data to being able to account for "all people everywhere (United Nations, 2016). Differences in the dynamic spatial distributions of hazards (Carrão, Naumann, & Barbosa, 2016; Oliveira, Oehler, San-Miguel-Ayanz, Camia, & Pereira, 2012), the spatial variation of the effects of climate change (Ericson, Vorosmarty, Dingman, Ward, & Meybeck, 2006; Hanjra & Qureshi, 2010; Stephenson et al., 2010), spatially allocating services to ensure sufficient coverage (Eckert & Kohler, 2014; Sverdlik, 2011), and targeting interventions and planning (Linard, Alegana, Noor, Snow, & Tatem, 2010; Utazi et al., 2018) based upon local context with limited resources requires more accurate mapping of BS and mapping of populations, both large and small (United Nations, 2016). Here we have shown a flexible modelling framework constructed from open-source methods and covariates to produce a framework that can be scaled to global extent across a variety of study areas and input data. This model approximates patterns of BS growth through time with good agreement for most years at the pixel and the units used in disaggregation (Table 4, Figures 4 and 6). Here we have shown the BSGM framework is capable of filling gaps of imagery-derived urban feature datasets by estimating the extents in between observations. This emphasizes the strength of using an interpolative model, such as BSGM, as opposed to more imagery dependent annual feature extraction methods that may encounter adverse atmospheric conditions, limited sensor revisits, or the need for more resource intensive imagery-based interpolation methods. This framework, and resultant output data, can be used for better modelling of population through time, inform future urban feature extraction from imagery, help facilitate intervention/planning/monitoring of development goals, and potentially serve as a platform for simulating different transition paths through time and investigating correlates of BS spatial growth.

However, the BSGM is neither without error not a total replacement for urban feature extractions. Given that the BSGM is interpolative, its predictions are limited by the accuracy, the spatial quality, and the temporal quality of its input urban feature dataset, the input time-specific subnational population data, and the input population surfaces. For example, the poorer model performance seen from 2001 through 2003 (Figures 4-8) are likely due to the fact the ESA data did not delineate changes, detected at 30 arc sec resolution, at 10 arc second resolution due to the MERIS and PROBA V imagery not being available (UCL Geomatics, 2017). With regards to total disagreement of the model (Figure 5), the relatively high contribution of allocation disagreement prior to circa 2010 and corresponding decrease in contribution post-2010 is likely due to the switch from using coarser DMSP-based LAN data to VIIRS-based LAN data at the 2012 time point.

Further, models are limited by their conceptual and mathematical assumptions. In this framework, we are assuming a certain relationship between relative population and population density changes and drive demand for temporally coincident settlement growth. This is not to say the assumed relationship is correct; here we assume BS population grows logistically with a time varying capacity that is temporally coincident, i.e. not lagged, and we assume BS population density follows a natural cubic spline across all observed points. This

Preprints (www.preprints.org) | NOT PEER-REVIEWED | Posted: 20 December 2018 doi:10.20944/preprints201812.0250.v1

is further predicated upon the assumption that the BS growth is predominantly driven by changes in population and or population density and the resulting demand is instantaneously filled as opposed to being delayed temporally. While there is support for population change being an empirical and theoretical driver of urban/BS growth (Angel et al., 2011; Dyson, 2011; Linard et al., 2013; Seto et al., 2011, 2012), there is also evidence for the use of other covariates, not used here because of their unavailability at subnational levels globally through time, such as Gross Domestic Product and arable land per capita (Angel et al., 2011; Seto et al., 2011). Furthermore, there are other "intangibles" such as local, regional, and national land use or development policies, which almost certainly shape BS growth, but are typically not in an accessible format, if available at all. The value of using population data to predict growth of settlement, shown here in a semi-independent model framework, and the value of using urban/settlement feature data sets to predict population distribution (Nieves et al., 2017), raises the question of whether it is worthwhile or proper to try to fully separate population and settlement given their reciprocal causal links, i.e. population begets built environment and settlement, settlement, typically, begets more population.

The modelling assumptions here are preceded by the assumption of exponential interpolation of annual population totals by the GPWv4-based data (Doxsey-Whitfield et al., 2015) and that the RF-informed dasymetric redistribution of those population totals are correctly locating the population in a manner which leads to correct BS population estimates for the BSGM to utilize. We already know that the RF population model tends to underestimate populations in BS and overestimate populations outside of urbanized areas (Stevens et al., 2015). Since the BSGM allocates transitions based upon relative changes in BS population, this last point should not affect prediction timings, assuming the RF-informed population modelling biases are consistent between the two times. Alternatively, any spatially explicit population datasets can be used as inputs for the BSGM, even the base GPW4, removing the need to use a modelled population input. With any area-based metric the Modifiable Areal Unit Problem (Openshaw, 1984) must be considered, as the total number of pixels in each unit is typically larger in the less settled areas resulting in less variation of aggregated metric values in those areas. With dasymetric redistribution methods, the size and configuration of the source units, spatially or temporally, can also affect the quality of the disaggregation with the larger relative differences between source unit and target unit sizes introducing more uncertainty to the output (Mennis, 2003; Mennis & Hultgren, 2006). As the concept of urban growth can be thought of as an incremental process, with future outcome dependent upon previous growth, the gridded outputs of the BSGM can be aggregated across years to decrease uncertainty of the interpolated extents should annual datasets not be needed.

5. CONCLUSIONS

As urban feature dataset producers such as ESA, MAUPP, GHSL, GUF and others continue to improve and release datasets with higher temporal resolution, models such as the BSGM will likely still have utility due to imagery/extraction issues and a need to smooth or fill-in time periods where difficulty was experienced (ESA CCI, 2017; T Esch et al., 2013; Forget, Linard, & Gilbert, 2018; Pesaresi et al., 2016). By the time annual urban feature extractions have filled the current demand and become the standard, there will have grown a demand for quarterly, monthly, and so on, feature extractions and an interpolative model will

 doi:10.20944/preprints201812.0250.v1

attempt to fill the need, data permitting, until the imagery and computational resources can. This is not to say that interpolative models and imagery-extracted features are oppositional, but rather are complementary. Should the time come where high-resolution annual feature datasets become the norm, this would offer a wealth of information from which to improve the model assumptions the BSGM currently makes. Further, the predictions of the BSGM could serve as a comparative check in the production of future urban feature extractions and a platform to explore population and BS dynamics.

As informative as urban feature extraction datasets are, imagery will never see into the future and we plan on extending this framework to allow for projection of BS growth, both in a predictive manner as well as allowing scenarios to be input. We found that the primary predictors of growth BS extents were related to connectivity, i.e. road networks, and local, i.e. ~0.5-1.5km, settlement density (Figure 3) both giving support to work in attempting to define "urban" base on contiguity, connectivity, and spatial density (Dijkstra & Poelman, 2014; T Esch et al., 2014; Pesaresi & Freire, 2016) and implying that investment in detecting/simulating new road network data would be beneficial to better predicting urban feature extents. Still mostly unknown is how the BSGM would perform for smaller settlements, not captured by coarser datasets such as the ESA land cover, and we are looking to test this with forthcoming feature data sets with resolutions below 3 arc seconds. Lastly, we plan to validate the utility of these dataset in an applied manner by comparing the effects of including the BSGM derived extents in annual population modelling.

Here we have presented an open source framework for interpolating a binary BS or urban feature dataset using a limited covariate dataset that can be used to further population mapping by filling a current gap in annual global urban feature datasets. This framework is scalable globally, but also allows for sub-study area variation in transition probability, population changes, and lights-at-night changes to drive the overall study area model. Further, the model can be adapted to run at other scales, both spatially and temporally, either by modifying the provided code or in many cases, simply by modifying the input data. The annual global interpolative and projected datasets from 2000 to 2020, produced with an early version of this model with a reduced covariate set, is freely available on the WorldPop website (worldpop.org) with the up to date model production code hosted on the WorldPop GitHub repository (github.com/wpgp/BSGMi_alpha). The specific model code used in producing this work is included in the supplementary material.

REFERENCES

Angel, S., Parent, J., Civco, D. L., Blei, A. M., & Potere, D. (2011). The Dimensions of Global Urban Expansion: Estimates and Projections for All Countries, 2000-2050. *Progress in Planning*, *75*, 53–107. https://doi.org/10.1016/j.progress.2011.04.001

Angel, S., Sheppard, S. C., & Civco, D. L. (2005). *The Dynamics of Global Urban Expansion*. Washington, D. C.: The World Bank.

Barredo, J. I., Demicheli, L., Lavalle, C., Kasanko, M., & McCormick, N. (2004). Modelling Future Urban Scenarios in Developing Countries: An Application Case Study in Lagos, Nigeria. *Environment and Planning B*, *31*, 65–84.

Bartholomé, E., & Belward, A. S. (2005). GLC2000: a new approach to global land cover mapping from Earth observation data. *International Journal of Remote Sensing*, *26*(9), 1959–1977. https://doi.org/10.1080/01431160412331291297

Batty, M. (2009). Urban Modeling. In *International Encyclopedia of Human Geography* (pp. 51–58). Oxford, UK: Elsevier.

Batty, M., & Xie, Y. (1994). From Cells to Cities. *Environment and Planning B*, *21*, S31–S48.

Booth, H. (2006). Demographic forecasting: 1980 to 2005 in review. *International Journal of Forecasting*, *22*(3), 547–581. https://doi.org/10.1016/j.ijforecast.2006.04.001

Breiman, L. (2001). Random Forests. *Machine Learning*, *45*(1), 5–32.

Carrão, H., Naumann, G., & Barbosa, P. (2016). Mapping global patterns of drought risk: An empirical framework based on sub-national estimates of hazard, exposure and vulnerability. *Global Environmental Change*, *39*, 108–124. https://doi.org/10.1016/j.gloenvcha.2016.04.012

Chongsuvivatwong, V., Phua, K. H., Yap, M. T., Pocock, N. S., Hashim, J. H., Chhem, R., … Lopez, A. D. (2011). Health and health-care systems in southeast Asia: diversity and transitions. *The Lancet*, *377*(9763), 429–437. https://doi.org/10.1016/S0140-6736(10)61507-3

Clarke, K. C., & Gaydos, L. (1998). Loose-coupling a Cellular Automaton Model and GIS: Long-term Urban Growth Prediction for San Francisco and Washington/Baltimore. *International Journal of Geographic Information Sciences*, *12*(7), 699–714.

Clarke, K. C., Hoppen, S., & Gaydos, L. (1997). A Self-modifying Cellular Automaton Model of Historical Urbanization in the San Francisco Bay Area. *Environment and Planning B*, *24*, 247–261.

Cohen, B. (2006). Urbanization in Developing Countries: Current Trends, Future Projections, and Key Challenges for Sustainability. *Technology in Society*, *28*, 63–80.

Cohen, J. E. (1995). Population Growth and Earth's Human Carrying Capacity. *Science*, *269*(5222), 341–346.

Dhingra, M. S., Artois, J., Robinson, T. P., Linard, C., Chaiban, C., Xenarios, I., … Gilbert, M. (2016). Global mapping of highly pathogenic avian influenza H5N1 and H5Nx clade 2.3.4.4 viruses with spatial cross-validation. *ELife*, *5*. https://doi.org/10.7554/eLife.19571

Dijkstra, L., & Poelman, H. (2014). *A harmonized definition of cities and rural areas: the new degree of urbanization* (Regional Working Paper No. WP 01/2014). Retrieved from http://ec.europa.eu/regional_policy/sources/docgener/work/2014_01_new_urban.pdf

Doxsey-Whitfield, E., MacManus, K., Adamo, S. B., Pistolesi, L., Squires, J., Borkovska, O., & Baptista, S. R. (2015). Taking advantage of the improved availability of census data: A first look at the Gridded Population of the World, Version 4. *Papers in Applied Geography*, *1*(3), 226–234. https://doi.org/10.1080/23754931.2015.1014272

Dyson, T. (2011). The role of the demographic transition in the process of urbanization. *Population and Development Review*, *37*(Supplement), 34–54.

Earth Observation Group NOAA National Geophysical Data Center. (2016). VIIRS Nighttime Lights - One Month Composites. Boulder, Colorado: NOAA National Centers for Environmental Information. Retrieved from https://ngdc.noaa.gov/eog/viirs/download_dnb_composites.html

Eckert, S., & Kohler, S. (2014). Urbanization and Health in Developing Countries: A Systematic Review. *World Health & Population*, *15*(1), 7–20.

Ericson, J. P., Vorosmarty, C. J., Dingman, S. L., Ward, L. G., & Meybeck, M. (2006). Effective sea-level rise and deltas: Causes of change and human dimension implications. *Global and Planetary Change*, *50*, 63–82.

ESA CCI. (2017). European Space Agency Climate Change Initiative Landcover. European Space Agency. Retrieved from http://maps.elie.ucl.ac.be/CCI/viewer/download.php

Esch, T., Bachofer, F., Heldens, W., Hirner, A., Marconcini, M., Palacios-Lopez, D., … Gorelick, N. (2018). Where We Live—A Summary of the Achievements and Planned Evolution of the Global Urban Footprint. *Remote Sensing*, *10*(6), 895. https://doi.org/10.3390/rs10060895

Esch, T., Marconcini, M., Felbier, A., Roth, A., Heldens, W., Huber, M., … Dech, S. (2013). Urban Footprint Processor - Fully Automated Processing Chain Generating Settlement Masks from Global Data of the TanDEM-X Mission. *IEEE Geoscience and Remote Sensing Letters*, *10*(6), 1617–1621.

Esch, T., Marconcini, M., Marmanis, D., Zeidler, J., Elsayed, S., Metz, A., & Dech, S. (2014). Dimensioning urbanization - An advanced procedure for characterizing human settlement properties using spatial network analysis. *Applied Geography*, *55*, 212–228. https://doi.org//j.apgeog.2014.09.009

Forget, Y., Linard, C., & Gilbert, M. (2018). Supervised Classification of Built-Up Areas in Sub-Saharan African Cities Using Landsat Imagery and OpenStreetMap. *Remote Sensing*, *10*(7), 1145. https://doi.org/10.3390/rs10071145

Gaughan, A. E., Stevens, F. R., Huang, Z., Nieves, J. J., Sorichetta, A., Lai, S., … Tatem, A. J. (2016). Spatiotemporal Patterns of Population in Mainland China, 1990 to 2010. *Scientific Data*, *3*, 160005. https://doi.org/10.1038/sdata.2016.5

Gaughan, A. E., Stevens, F. R., Linard, C., Jia, P., & Tatem, A. J. (2013). High Resolution Population Distribution Maps for Southeast Asia in 2010 and 2015. *PLoS One*, *8*(2), e55882. https://doi.org/10.1371/journal.pone.0055882

Goldewijk, K. K., Beusen, A., & Janssen, P. (2010). Long-term dynamic modeling of global population and built-up area in a spatially explicit way: HYDE 3.1. *The Holocene*, *20*(4), 565–573. https://doi.org/10.1177/0959683609356587

Haibo He, & Garcia, E. A. (2009). Learning from Imbalanced Data. *IEEE Transactions on Knowledge and Data Engineering*, *21*(9), 1263–1284. https://doi.org/10.1109/TKDE.2008.239

Hanjra, M. A., & Qureshi, M. E. (2010). Global Water Crisis and Future Food Security in an Era of Climate Change. *Food Policy*, *35*, 365–377. https://doi.org/10.1016/j.foodpol.2010.05.006

He, H., & Garcia, E. A. (2009). Learning from Imbalanced Data, *21*(9), 1263–1284.

Hijmans, R. J., Cameron, S. E., Parra, J. L., Jones, P. G., & Jarvis, A. (2005). Very high resolution interpolated climate surfaces for global land areas. *International Journal of Climatology*, *25*, 1965–1978.

Lamarche, C., Santoro, M., Bontemps, S., D'Andrimont, R., Radoux, J., Giustarini, L., … Arino, O. (2017). Compilation and Validation of SAR and Optical Data Products for a Complete and Global Map of Inland/Ocean Water Tailored to the Climate Modeling Community. *Remote Sensing*, *9*(36). https://doi.org/10.3390/rs9010036

Leao, S., Bishop, I., & Evans, D. (2004). Simulating Urban Growth in a Developing Nation's

Region Using a Cellular Automata-based Model. *Journal of Urban Planning and Development*, *130*(3), 145–158.

Lehner, B., Verdin, K., & Jarvis, A. (2008). New Global Hydrography Derived from Spaceborne Elevation Data. *Eos, Transactions of the American Geophysical Union*, *89*(10), 93–94. https://doi.org/10.1029/2008EO100001

Linard, C., Alegana, V., Noor, A. M., Snow, R. W., & Tatem, A. J. (2010). A high resolution spatial population database of somolia for disease risk mapping. *International Journal of Health Geographics*, *9*(1), 45.

Linard, C., Tatem, A. J., & Gilbert, M. (2013). Modelling Spatial Patterns of Urban Growth in Africa. *Applied Geography*, *44*, 23–32.

McGranahan, G., Balk, D., & Anderson, B. (2007). The Rising Tide: Assessing the Risks of Climate Change and Human Settlements in Low Elevation Coastal Zones. *Environment & Urbanization*, *19*(1), 17–37. https://doi.org/10.1177/0956247807076960

McNeil, D. R., Trussell, T. J., & Turner, J. C. (1977). Spline Interpolation of Demographic Data. *Demography*, *14*(2), 245–252. Retrieved from https://www.jstor.org/stable/2060581

Mennis, J. (2003). Generating surface models of population using dasymetric mapping. *Professional Geographer*, *55*(1), 31–42.

Mennis, J., & Hultgren, T. (2006). Intelligent dasymetric mapping and its application to areal interpolation. *Cartography and Geographic Information Science2*, *33*, 179–194.

Meyer, P. S., & Ausubel, J. H. (1999). Carrying capacity: A model with logistically varying limits. *Technological Forecasting and Social Change*, *61*(3), 209–214. https://doi.org/10.1016/S0040-1625(99)00022-0

Nelson, A. (2008). Estimated Travel Time to the Nearest city of 50,000 or More People in Year 2000. Ispra, Italy: Global Environment Monitoring Unit - Joint Research Centre of the European Commission. Retrieved from http://forobs.jrc.ec.europa.eu/products/gam/sources.php

Nieves, J. J., Stevens, F. R., Gaughan, A. E., Linard, C., Sorichetta, A., Hornby, G., … Tatem, A. J. (2017). Examining the correlates and drivers of human population distributions across low- and middle-income countries. *Journal of The Royal Society Interface*, *14*(137), 20170401. https://doi.org/10.1098/rsif.2017.0401

Oliveira, S., Oehler, F., San-Miguel-Ayanz, J., Camia, A., & Pereira, J. M. C. (2012). Modeling spatial patterns of fire occurrence in Mediterranean Europe using Multiple Regression and Random Forest. *Forest Ecology and Management*, *275*(July 2012), 117–129. https://doi.org/10.1016/j.foreco.2012.03.003

Openshaw, S. (1984). The modifiable areal unit problem. *Concepts and Techniques in Modern Geography*, *38*.

OpenStreetMap Contributers. (2017). OpenStreetMap (OSM) Database. OSM. Retrieved from openstreetmap.org

Patel, N., Angiuli, E., Gamba, P., Gaughan, A. E., Lisini, G., Stevens, F. R., … Trianni, G. (2015). Multitemporal Settlement and Population Mapping From Landsat Using Google Earth Engine. *International Journal of Applied Earth Observation and Geoinformation*, *35*(Part B), 199–208. https://doi.org/10.1016/j.jag.2014.09.005

Pesaresi, M., Ehrlich, D., Ferri, S., Florczyk, A. J., Freire, S., Halkia, S., … Syrris, V. (2016). *Operating Procedure for the Production of the Global Human Settlement Layer from Landsat Data of the Epochs 1975, 1990, 2000, and 2014*. Publications Office of the European Union. Retrieved from doi: 10.2788/253582

Pesaresi, M., & Freire, S. (2016). GHS settlement grid, following the REGIO model 2014 in application to GHSL Landsat and CIESIN GPW v4-multitemporal (1975-1990-2000-2015). Retrieved October 26, 2018, from http://data.jrc.ec.europa.eu/dataset/jrc-ghsl-

ghs_smod_pop_globe_r2016a

Pesaresi, M., Guo, H., Blaes, X., Ehrlich, D., Ferri, S., Gueguen, L., … Zanchetta, L. (2013). A Global Human Settlement Layer from Optical HR/VHR Remote Sensing Data: Concept and First Results. *IEEE Journal of Selected Topics in Applied Earth Observation & Remote Sensing*, *6*(5), 2102–2131. https://doi.org/10.1109/JSTARS.2013.2271445

Pontius, R. G., & Millones, M. (2011). Death to Kappa: birth of quantity disagreement and allocation disagreement for accuracy assessment. *International Journal of Remote Sensing*, *32*(15), 4407–4429. https://doi.org/10.1080/01431161.2011.552923

Potere, D., & Schneider, A. (2007). A critical look at representations of urban areas in global maps. *GeoJournal*, *69*(1–2), 55–80. https://doi.org/10.1007/s10708-007-9102-z

Potere, D., Schneider, A., Angel, S., & Civco, D. (2009). Mapping urban areas on a global scale: which of the eight maps now available is more accurate? *International Journal of Remote Sensing*, *30*(24), 6531–6558. https://doi.org/10.1080/01431160903121134

R Core Team. (2016). R: A Language and Environment Layer for Statistical Computing. Vienna, Austria: R Foundation for Statistical Computing. Retrieved from https://www.r-project.org

Rogan, W. J., & Gladen, B. (1978). Estimating prevalence from the results of a screening test. *American Journal of Epidemiology*, *107*(1), 71–76.

Saito, T., & Rehmsmeier, M. (2015). The Precision-Recall Plot is More Informative than the ROC Plot When Evaluating Binary Classifiers on Imbalanced Datasets. *PLoS One*, *10*(3), e0118432. https://doi.org/10.1371/journal.pone.0118432

Sante, I., Garcia, A. M., Miranda, D., & Crecente, R. (2010). Cellular Automata Models for the Simulation of Real-world Urban Processes: A Review and Analysis. *Landscape and Urban Planning*, *96*, 108–122. https://doi.org/10.1016/j.landurbplan.2010.03.001

Schneider, A., Friedl, M. A., McIver, D. K., & Woodcock, C. E. (2003). Mapping Urban Areas by Fusing Multiple Sources of Coarse Resolution Remotely Sensed Data. *Photogrammetry & Remote Sensing*, *69*(12), 1377–1386.

Schneider, A., Friedl, M. A., & Potere, D. (2010). Mapping Urban Areas Using MODIS 500-m Data: New Methods and Datasets Based on "Urban Ecoregions." *Remote Sensing of the Environment*, *114*, 1733–1746.

Schneider, A., & Woodcock, C. E. (2008). Compact, Dispersed, Fragmented, Extensive? A Comparison of Urban Growth in Twenty-five Global Cities using Remotely Sensed Data, Pattern Metrics and Census Information. *Urban Studies*, *45*(3), 659–692. https://doi.org/10.1177/0042098007087340

Seto, K. C., Fragkias, M., Guneralp, B., & Reilly, M. K. (2011). A Meta-Analysis of Global Urban Land Expansion. *PLoS One*, *6*(8), e23777. https://doi.org/10.1371/journal.pone.0023777

Seto, K. C., Guneralp, B., & Hutyra, L. R. (2012). Global Forecasts of Urban Expansion to 2030 and Direct Impacts on Biodiversity and Carbon Pools. *Proceedings of the National Academy of Sciences of the United States of America*, *109*(40), 16083–16088. https://doi.org/10.1073/pnas.1211658109

Sibly, R. M. (2005). On the Regulation of Populations of Mammals, Birds, Fish, and Insects. *Science*, *309*(5734), 607–610. https://doi.org/10.1126/science.1110760

Small, C. (2009). The color of cities:An overview of urban spectral diversity. In M. Herold & P. Gamba (Eds.), *Global Mapping of Human Settlements* (pp. 59–106). New York: Taylor & Francis.

Stephenson, J., Newman, K., & Mayhew, S. (2010). Population dynamics and climate change: What are the links? *Journal of Public Health*, *32*(2), 150–156. https://doi.org/10.1093/pubmed/fdq038

Stevens, F. R., Gaughan, A. E., Linard, C., & Tatem, A. J. (2015). Disaggregating Census Data for Population Mapping Using Random Forests with Remotely-sensed Data and Ancillary Data. *PLoS One*, *10*(2), e0107042. https://doi.org/10.1371/journal.pone.0107042

Sverdlik, A. (2011). Ill-health and poverty: A literature review on health in informal settlements. *Environment and Urbanization*, *23*(1), 123–155. https://doi.org/10.1177/0956247811398604

Tayyebi, A., Pekin, B. K., Pijanowski, B. C., Plourde, J. D., Doucette, J. S., & Braun, D. (2013). Hierarchical modeling of urban growth across the conterminous USA: Developing meso-scale quantity drivers for the Land Transformation Model. *Journal of Land Use Science*, *8*(4), 422–442. https://doi.org/10.1080/1747423X.2012.675364

U.N. Enviroment Programme World Conservation Monitoring Centre, & IUCN World Commission on Protected Areas. (2015, November 7). World Database on Protected Areas. IUCN & UNEP. Retrieved from https://www.protectedplanet.net/

UCL Geomatics. (2017). *Land Cover CCI Product User Guide Version 2.0*. Retrieved from http://maps.elie.ucl.ac.be/CCI/viewer/download/ESACCI-LC-Ph2-PUGv2_2.0.pdf

United Nations. (2015). *World Urbanization Prospects: The 2014 Revision* (World Urbanization Prospects No. ST/ESA/SER.A/366). New York, New York: United Nations, Dept. of Economic and Social Affairs.

United Nations. (2016). *Transforming Our World: The 2030 Agenda for Sustainable Development*.

Utazi, C. E., Thorley, J., Alegana, V. A., Ferrari, M. J., Takahashi, S., Metcalf, C. J. E., … Tatem, A. J. (2018). High resolution age-structured mapping of childhood vaccination coverage in low and middle income countries. *Vaccine*, *36*(12), 1583–1591. https://doi.org/10.1016/j.vaccine.2018.02.020

Verburg, P. H., Schot, P. P., Dijst, M. J., & Veldkamp, A. (2004). Landuse Change Modelling: Current Practice and Research Priorities. *GeoJournal*, *61*, 309–324.

Verburg, P. H., Soepboer, W., Veldkamp, A., Limpiada, R., Espladon, V., & Mastura, S. S. A. (2002). Modeling the Spatial Dynamics of Regional Land Use: The CLUE-S Model. *Environmental Management*, *30*(3), 391–405. https://doi.org/10.1007/s00267-002-2630-x

Weiss, D. J., Nelson, A., Gibson, H. S., Temperley, W., Peedell, S., Lieber, A., … Gething, P. W. (2018). A global map of travel time to cities to assess inequalities in accessibility in 2015. *Nature*, *553*(7688), 333–336. https://doi.org/10.1038/nature25181

White, R., & Engelen, G. (1997). Cellular Automata as the Basis of Integrated Dynamic Regional Modelling. *Environment and Planning B*, *24*, 235–246.

White, R., & Engelen, G. (2000). High Resolution Modelling of the Spatial Dynamics of Urban and Regional Systems. *Computers, Environment, and Urban Systems*, *24*(383–400).

WorldPop, S. of G. and E. S. U. of, Department of Geography and Geosciences, U. of L., Département de Géographie, U. de N., & Center for International Earth Science Information Network (CIESIN), C. U. (2018). Global High Resolution Population Denominators Project. Bill and Melinda Gates Foundation (OPP1134076). https://doi.org/10.5258/SOTON/WP00644

Zhang, Q., Pandey, B., & Seto, K. C. (2016). A Robust Method to Generate a Consistent Time Series From DMSP/OLS Nighttime Light Data. *IEEE Transactions on Geoscience and Remote Sensing*, *54*(10), 5821–5831. https://doi.org/10.1109/TGRS.2016.2572724